....
....

Solution of Two-Dimensional Riemann Problems for Gas Dynamics without Riemann Problem Solvers

Alexander Kurganov† and Eitan Tadmor‡

August 16, 2000

Abstract

We report here on our numerical study of the two-dimensional Riemann problem for the compressible Euler equations. Compared with the relatively simple 1-D configurations, the 2-D case consists of a plethora of geometric wave patterns which pose a computational challenge for high-resolution methods. The main feature in the present computations of these 2-D waves is the use of the Riemann-solvers-free central schemes presented in [10]. This family of central schemes avoids the intricate and time-consuming computation of the eigensystem of the problem, and hence offers a considerably simpler alternative to upwind methods. The numerical results illustrate that despite their simplicity, the central schemes are able to recover with comparable high-resolution, the various features observed in the earlier, more expensive computations.

AMS subject classification: Primary 65M10; Secondary 65M05

Key Words: Multidimensional conservation laws, Euler equations of gas dynamics, Riemann problem, semi-discrete central schemes, non-oscillatory piecewise polynomial reconstructions.

Contents

1 Introduction **1**

2 Genuinely multidimensional semi-discrete central schemes **2**
2.1 Fully-discrete central schemes 2
2.2 The semi-discrete limit 5

3 Numerical experiments **8**

1 Introduction

We report here on our numerical study of two-dimensional (2-D) Riemann problem for the compressible Euler equations, following the works of Schultz-Rinne et. al. [24, 25], Chang et. al. [1], Zhang & Zheng [30], Lax & Liu [16], and Chang et. al [2].

Before turning to the 2-D case, we recall the corresponding one-dimensional setup. The one-dimensional (1-D) Riemann problem could be solved in terms of a succession of centered waves, [15]. In particular, the 1-D centered waves associated with gas dynamics equations consist of shock-, rarefaction- and contact-waves, [3, 15, 28]. The exact (or approximate) 1-D Riemann problem solvers serve as

†Department of Mathematics, University of Michigan, Ann Arbor, MI 48109. Email: kurganov@math.lsa.umich.edu
‡Department of Mathematics, UCLA, Los Angeles, CA 90095. Email: tadmor@math.ucla.edu

a building block for the large class of so-called *upwind schemes*, following the seminal work of Godunov [3]. The other class of so-called *central schemes* offers an alternative to upwind methods by avoiding the time-consuming computation of (approximate) Riemann problem solvers, yet retaining the desired high-resolution. Unlike the 1-D case, however, no explicit Riemann solvers are available in the two-dimensional case. Indeed, the 2-D Riemann problem separated by 1-D elementary waves offers a plethora of no less than 19 different admissible configurations [1, 16, 30, 24, 25, 2], which therefore cannot be utilized as a building block in the two-dimensional case. Consequently, 2-D upwind schemes require some sort of dimensional splitting, where 1-D Riemann problems are solved, one dimension at the time. The advantage of the Riemann-solvers-free central schemes is therefore further amplified in the 2-D case. By avoiding the intricate and time-consuming computation of the eigen-structures in one- and in particular, two-dimensional problems, we end up with a considerably simpler and faster class of high-resolution schemes.

Central schemes can be formulated along the lines of the original Godunov's framework, [3], namely, realizing the evolution of piecewise polynomial solution after each small time step by its cell averages. To avoid Riemann problem solvers, however, the solution of central schemes is realized by cell averages computed over *staggered* cells, which in turn yield numerical fluxes located inside the smooth part of the piecewise solution. In the original 1-D second-order central scheme of Nessyahu and Tadmor [23], and its higher-order and 2-D generalizations [21, 6], cells of typical spatial length Δx were staggered in alternate time steps, by being placed $\Delta x/2$ away from each other. In the more recent, less dissipative versions of central schemes presented in [13, 9, 11, 10, 12], staggered cells were placed in a distance of order $\mathcal{O}(\Delta t)$ from each other. The latter versions admit a particularly simple semi-discrete limit by letting $\Delta t \downarrow 0$. Consequently, alternating cells collapse onto each other in the semi-discrete limit and staggering is avoided altogether. Let us also mention that there are other derivations of central schemes, most notably, as limits of relaxation methods [7] or by flux splitting [22].

In Section 2 we provide a brief description of the central schemes proposed in [10], which have been applied to the two-dimensional Euler equations of gas dynamics in Section 3. Compared with the 'simple' 1-D configurations, the 2-D case offers 19 different configurations which consist of a considerably richer variety of 2-D geometric patterns formed by shocks, rarefactions, slip lines, and contacts. The main feature of the present computation is the use of Riemann-solvers-free central schemes to resolve this variety of wave formations. Remarkably, the numerical results reported in Section 3 show that despite the lack of any specific 'physical' input beyond the maximal local speeds, the central schemes recover with a comparable high-resolution, *all* the features observed by the earlier, more expensive computations based on upwind schemes.

2 Genuinely multidimensional semi-discrete central schemes

2.1 Fully-discrete central schemes

We consider a general two-dimensional system of hyperbolic conservation laws,

$$u_t + f(u)_x + g(u)_y = 0. \tag{2.1}$$

The computed solution is realized in terms of the cell averages

$$\bar{u}^n_{j,k} := \frac{1}{\Delta x \Delta y} \int\limits_{x_{j-\frac{1}{2}}}^{x_{j+\frac{1}{2}}} \int\limits_{y_{k-\frac{1}{2}}}^{y_{k+\frac{1}{2}}} u(x,y,t^n)\,dx\,dy,$$

based on spatial cells $I_{jk} = [x_{j-\frac{1}{2}}, x_{j+\frac{1}{2}}] \times [y_{k-\frac{1}{2}}, y_{k+\frac{1}{2}}]$. Here and below, $(x_\alpha, y_\beta) = (\alpha\Delta x, \beta\Delta y)$ denote the coordinates of the computational grid. To advance the computation to the next time level at $t = t^{n+1}$, we proceed with three steps of *reconstruction, evolution* and *projection.*

Starting with the given cell averages $\bar{u}^n_{j,k}$, the first step consists of *reconstructing* a non-oscillatory piecewise polynomial of the form

$$\widetilde{u}^n(x,y) := \sum_{j,k} p^n_{j,k}(x,y)\chi_{I_{jk}}(x,y), \tag{2.2}$$

where the χ's are the characteristic functions of the corresponding intervals. Different choices of polynomial reconstructions result in different types of central schemes. Few choices will be outlined below in (2.5),(2.6). In the second step, we *evolve* the piecewise polynomial $\tilde{u}^n(x,y)$ in time by solving the initial-value problem (2.1),(2.2). Each of the polynomial pieces of $\widetilde{u}^n(x,y)$ centered around the vertices $(x_{j\pm\frac{1}{2}}, y_{k\pm\frac{1}{2}})$ is propagated within a 'rectangular cone' of influence, $D_{j\pm\frac{1}{2},k\pm\frac{1}{2}}$, whose boundaries propagate with different right- and left-sided *local speeds*, consult the floor plan in Figure 2.1. The computed values of the local speeds $a^\pm_{j+\frac{1}{2},k}, b^\pm_{j,k+\frac{1}{2}}$ are specified below at (2.8).

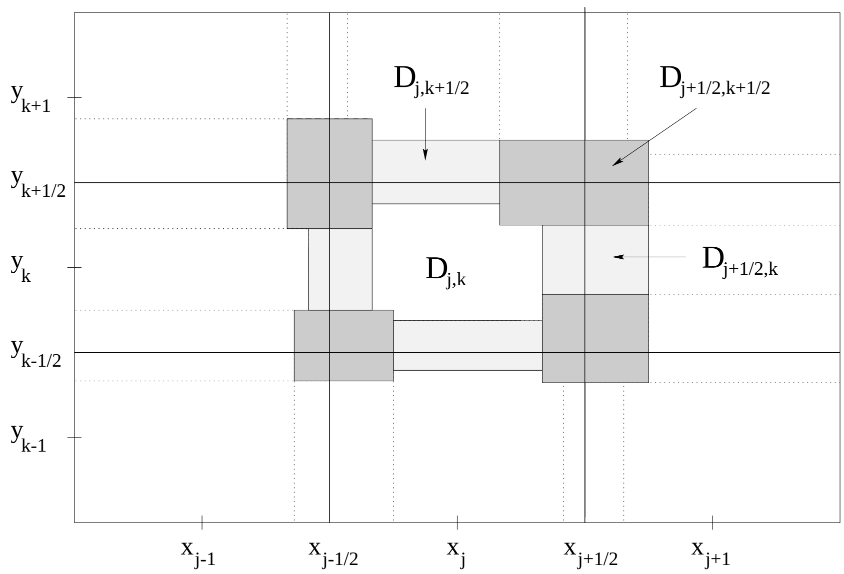

Figure 2.1: Two-dimensional central-upwind differencing

Integrating (2.1),(2.2) over rectangular control volumes erected under the aforementioned domains, $D_{\alpha\beta} \times [t^n, t^{n+1}]$, results in the new cell averages at time $t = t^{n+1}$, which are denoted, respectively, by $\{\bar{w}^{n+1}_{j,k+\frac{1}{2}}\}$, $\{\bar{w}^{n+1}_{j+\frac{1}{2},k}\}$, $\{\bar{w}^{n+1}_{j+\frac{1}{2},k+\frac{1}{2}}\}$ and $\{\bar{w}^{n+1}_{j,k}\}$. These cell averages can be computed explicitly following the approach in [6], using appropriate quadrature rules to approximate the flux across the temporal interfaces, consult [10] for details.

At this stage we end up with an approximate solution at $t = t^{n+1}$ of the form

$$\begin{aligned}\widetilde{w}^{n+1}(x,y) := \sum_{j,k} \Big[& \widetilde{w}^{n+1}_{j,k}\chi_{D_{jk}}(x,y) + \widetilde{w}^{n+1}_{j+\frac{1}{2},k}\chi_{D_{j+\frac{1}{2},k}}(x,y) + \\ & + \widetilde{w}^{n+1}_{j,k+\frac{1}{2}}\chi_{D_{j,k+\frac{1}{2}}}(x,y) + \widetilde{w}^{n+1}_{j+\frac{1}{2},k+\frac{1}{2}}\chi_{D_{j+\frac{1}{2},k+\frac{1}{2}}}(x,y)\Big].\end{aligned}$$

Finally, we conclude by *projecting* this computed solution back onto the original cells, which is again realized in terms of the cell averages

$$\bar{u}_{j,k}^{n+1} = \frac{1}{\Delta x \Delta y} \int\limits_{x_{j-\frac{1}{2}}}^{x_{j+\frac{1}{2}}} \int\limits_{y_{k-\frac{1}{2}}}^{y_{k+\frac{1}{2}}} \widetilde{w}^{n+1}(x,y)\,dxdy. \tag{2.3}$$

The above derivation results in the second- or third-order *fully-discrete* central schemes, with explicit yet complicated formulae. A particular advantage of these type of central schemes, compared with the original staggered version of central schemes introduced in [6], is the simplification that could be achieved by taking a semi-discrete limit, letting $\Delta t \downarrow 0$.

2.2 The semi-discrete limit

Following the approach in [13, 11, 10], we consider the central algorithm described above and pass to the limit as $\Delta t \to 0$. Notice that the cone of influence, $D_{jk} \times [t^n, t^n + \Delta t]$, falls back onto the original cell, I_{jk}, we have started with at $t = t^n$.

The resulting semi-discrete scheme can be written in the conservative form (see [10] for the detailed derivation),

$$\frac{d}{dt}\bar{u}_{j,k}(t) = -\frac{H^x_{j+\frac{1}{2},k}(t) - H^x_{j-\frac{1}{2},k}(t)}{\Delta x} - \frac{H^y_{j,k+\frac{1}{2}}(t) - H^y_{j,k-\frac{1}{2}}(t)}{\Delta y}. \tag{2.4}$$

Here, the numerical fluxes are obtained using a quadrature formula of an appropriate order for approximating the integrals across the interfaces of the domains $D_{j\pm\frac{1}{2},k}$ and $D_{j,k\pm\frac{1}{2}}$. We consider few examples.

• A second-order method. A second order method requires a piecewise linear reconstruction, (2.2), of the form

$$p^n_{j,k}(x,y) = \bar{u}^n_{j,k} + (u_x)^n_{j,k}(x - x_j) + (u_y)^n_{j,k}(y - y_k). \tag{2.5}$$

Here, $(u_x)^n_{j,k}$ and $(u_y)^n_{j,k}$ stand for an (at least first-order) approximation to the derivatives $u_x(x_j, y_k, t^n)$ and $u_y(x_j, y_k, t^n)$, respectively. To ensure a non-oscillatory nature of the reconstruction (2.2)–(2.5), one needs to employ a nonlinear limiter in the computation of these slopes. This can be done in many different ways (see, e.g., [4, 5, 8, 29]). In this paper, we have used van-Leer's one-parameter family of the minmod limiters, [17, 4, 29],

$$\begin{aligned}
(u_x)_{j,k} &= \text{minmod}\left(\theta\frac{\bar{u}_{j+1,k} - \bar{u}_{j,k}}{\Delta x}, \frac{\bar{u}_{j+1,k} - \bar{u}_{j-1,k}}{2\Delta x}, \theta\frac{\bar{u}_{j,k} - \bar{u}_{j-1,k}}{\Delta x}\right),\\
(u_y)_{j,k} &= \text{minmod}\left(\theta\frac{\bar{u}_{j,k+1} - \bar{u}_{j,k}}{\Delta y}, \frac{\bar{u}_{j,k+1} - \bar{u}_{j,k-1}}{2\Delta y}, \theta\frac{\bar{u}_{j,k} - \bar{u}_{j,k-1}}{\Delta y}\right),
\end{aligned} \tag{2.6}$$

where $\theta \in [1, 2]$, and the multivariable minmod function is defined by

$$\text{minmod}(x_1, x_2, ...) := \begin{cases} \min_j\{x_j\}, & \text{if } x_j > 0 \ \ \forall j, \\ \max_j\{x_j\}, & \text{if } x_j < 0 \ \ \forall j, \\ 0, & \text{otherwise.} \end{cases}$$

Remark. Notice that in the scalar case, larger θ's in (2.6) correspond to less dissipative, but still *non-oscillatory* limiters, [6, 13, 11, 10]. For systems of conservation laws, no proof of a non-oscillatory property is available. Nevertheless, a large variety of computations performed with central schemes

confirm stability and lack of spurious oscillations while achieving high-resolution throughout the computational domain. In particular, central schemes owe their considerable simplicity to implementation of the minmod limiter (2.6) *componentwise*; no need for eigen-decomposition of the vectors of divided differences. Our numerical experiments (Section 3, see also [11, 10, 13]) indicate that the optimal values of θ vary between 1 and 1.5.
Given the piecewise linear polynomial we can compute the reconstructed values at the interfaces

$$u^{\rm N}_{j,k} := p^n_{j,k}(x_j, y_{k+\frac{1}{2}}), \quad u^{\rm S}_{j,k} := p^n_{j,k}(x_j, y_{k-\frac{1}{2}}), \quad u^{\rm E}_{j,k} := p^n_{j,k}(x_{j+\frac{1}{2}}, y_k), \quad u^{\rm W}_{j,k} := p^n_{j,k}(x_{j-\frac{1}{2}}, y_k). \tag{2.7}$$

These interfaces are moving with the corresponding speeds

$$\begin{aligned}
a^+_{j+\frac{1}{2},k} &:= \max\left\{\lambda_N\Big(\frac{\partial f}{\partial u}(u^{\rm W}_{j+1,k})\Big), \lambda_N\Big(\frac{\partial f}{\partial u}(u^{\rm E}_{j,k})\Big), 0\right\},\\
b^+_{j,k+\frac{1}{2}} &:= \max\left\{\lambda_N\Big(\frac{\partial g}{\partial u}(u^{\rm S}_{j,k+1})\Big), \lambda_N\Big(\frac{\partial g}{\partial u}(u^{\rm N}_{j,k})\Big), 0\right\},\\
a^-_{j+\frac{1}{2},k} &:= \min\left\{\lambda_1\Big(\frac{\partial f}{\partial u}(u^{\rm W}_{j+1,k})\Big), \lambda_1\Big(\frac{\partial f}{\partial u}(u^{\rm E}_{j,k})\Big), 0\right\},\\
b^-_{j,k+\frac{1}{2}} &:= \min\left\{\lambda_1\Big(\frac{\partial g}{\partial u}(u^{\rm S}_{j,k+1})\Big), \lambda_1\Big(\frac{\partial g}{\partial u}(u^{\rm N}_{j,k})\Big), 0\right\},
\end{aligned} \tag{2.8}$$

where λ_N and λ_1 denote the largest and the smallest eigenvalues of the Jacobians $\frac{\partial f}{\partial u}$ and $\frac{\partial g}{\partial u}$, respectively.
Using second-order midpoint rule to approximate the spatial integrals along the faces of side cells, $D_{j+\frac{1}{2},k}$ and $D_{j,k+\frac{1}{2}}$, results in the second-order numerical fluxes

$$H^x_{j+\frac{1}{2},k} = \frac{a^+_{j+\frac{1}{2},k} f(u^{\rm E}_{j,k}) - a^-_{j+\frac{1}{2},k} f(u^{\rm W}_{j+1,k})}{a^+_{j+\frac{1}{2},k} - a^-_{j+\frac{1}{2},k}} + \frac{a^+_{j+\frac{1}{2},k} a^-_{j+\frac{1}{2},k}}{a^+_{j+\frac{1}{2},k} - a^-_{j+\frac{1}{2},k}} \Big[u^{\rm W}_{j+1,k} - u^{\rm E}_{j,k}\Big], \tag{2.9}$$

and

$$H^y_{j,k+\frac{1}{2}} = \frac{b^+_{j,k+\frac{1}{2}} g(u^{\rm N}_{j,k}) - b^-_{j,k+\frac{1}{2}} g(u^{\rm S}_{j,k+1})}{b^+_{j,k+\frac{1}{2}} - b^-_{j,k+\frac{1}{2}}} + \frac{b^+_{j,k+\frac{1}{2}} b^-_{j,k+\frac{1}{2}}}{b^+_{j,k+\frac{1}{2}} - b^-_{j,k+\frac{1}{2}}} \Big[u^{\rm S}_{j,k+1} - u^{\rm N}_{j,k}\Big]. \tag{2.10}$$

Remark. The computation in (2.8) takes into account the different local speeds from each side of the x- and y-interfaces. If we further simplified by using a *symmetric* cone of propagation with local speeds $a^{\pm}_{j+\frac{1}{2},k} := \pm\max\{|a^+_{j+\frac{1}{2},k}|, |a^-_{j+\frac{1}{2},k}|\}$, $b^{\pm}_{j,k+\frac{1}{2}} := \pm\max\{|b^+_{j,k+\frac{1}{2}}|, |b^-_{j,k+\frac{1}{2}}|\}$, then the central scheme (2.4),(2.9)–(2.10) is reduced to the central scheme introduced earlier in [13]. The refinement, introduced in [10], requires a more precise cone of propagation, which nevertheless avoids any additional information on the eigen-structure of the problem.

• An alternative second-order method. With the same piecewise linear reconstruction as before, (2.5), we introduce the corner values

$$u^{\rm NE(NW)}_{j,k} := p^n_{j,k}(x_{j\pm\frac{1}{2}}, y_{k+\frac{1}{2}}), \quad u^{\rm SE(SW)}_{j,k} := p^n_{j,k}(x_{j\pm\frac{1}{2}}, y_{k-\frac{1}{2}}), \tag{2.11}$$

Replacing the second-order midpoint rule with the trapezoidal rule gives the alternative second-order numerical fluxes,

$$\begin{aligned}
H^x_{j+\frac{1}{2},k} \;:=\;& \frac{a^+_{j+\frac{1}{2},k}}{2(a^+_{j+\frac{1}{2},k} - a^-_{j+\frac{1}{2},k})}\Big[f(u^{\rm NE}_{j,k}) + f(u^{\rm SE}_{j,k})\Big] - \frac{a^-_{j+\frac{1}{2},k}}{2(a^+_{j+\frac{1}{2},k} - a^-_{j+\frac{1}{2},k})}\Big[f(u^{\rm NW}_{j+1,k}) + f(u^{\rm SW}_{j+1,k})\Big] + \\
&+ \frac{a^+_{j+\frac{1}{2},k} a^-_{j+\frac{1}{2},k}}{2(a^+_{j+\frac{1}{2},k} - a^-_{j+\frac{1}{2},k})}\Big[u^{\rm NW}_{j+1,k} - u^{\rm NE}_{j,k} + u^{\rm SW}_{j+1,k} - u^{\rm SE}_{j,k}\Big],
\end{aligned} \tag{2.12}$$

and

$$H^y_{j,k+\frac{1}{2}} := \frac{b^+_{j,k+\frac{1}{2}}}{2(b^+_{j,k+\frac{1}{2}}-b^-_{j,k+\frac{1}{2}})}\Big[g(u^{\rm NW}_{j,k})+g(u^{\rm NE}_{j,k})\Big]-\frac{b^-_{j,k+\frac{1}{2}}}{2(b^+_{j,k+\frac{1}{2}}-b^-_{j,k+\frac{1}{2}})}\Big[g(u^{\rm SW}_{j,k+1})+g(u^{\rm SE}_{j,k+1})\Big]+$$
$$+\frac{b^+_{j,k+\frac{1}{2}}b^-_{j,k+\frac{1}{2}}}{2(b^+_{j,k+\frac{1}{2}}-a^-_{j,k+\frac{1}{2}})}\Big[u^{\rm SW}_{j,k+1}-u^{\rm NW}_{j,k}+u^{\rm SE}_{j,k+1}-u^{\rm NE}_{j,k}\Big]. \tag{2.13}$$

Remark. The numerical fluxes in (2.12) and (2.13) offer a genuinely multidimensional discretization by adding the cross diagonal directions to the Cartesian directions utilized in (2.8).

• A third-order method. The third-order scheme is based on a reconstruction of a non-oscillatory piecewise quadratic polynomial. One of the possible ways to obtain an essentially non-oscillatory third-order reconstruction is by using a weighted ENO approach (see the reconstructions presented in [18, 19]). The disadvantage of the ENO-type interpolants is that they are based on smoothness indicators, and thus on an a-priori information about the solution, which may be unavailable. This may result in spurious oscillations or extra smearing of discontinuities.

In this paper, we have used an alternative reconstruction, which was proposed in [11]. The main idea is to apply one-dimensional non-oscillatory piecewise quadratic interpolants (for examples of such one-dimensional reconstructions we refer the reader to [20, 21, 11]) in the x- and y-directions, and in the diagonal directions. The detailed description of this two-dimensional extension can be found in [11], see also [10].

The numerical fluxes, which correspond to the fourth-order Simpson's quadrature rule, are

$$\begin{aligned}H^x_{j+\frac{1}{2},k} &:= \frac{a^+_{j+\frac{1}{2},k}}{6(a^+_{j+\frac{1}{2},k}-a^-_{j+\frac{1}{2},k})}\Big[f(u^{\rm NE}_{j,k})+4f(u^{\rm E}_{j,k})+f(u^{\rm SE}_{j,k})\Big]-\\ &-\frac{a^-_{j+\frac{1}{2},k}}{6(a^+_{j+\frac{1}{2},k}-a^-_{j+\frac{1}{2},k})}\Big[f(u^{\rm NW}_{j+1,k})+4f(u^{\rm W}_{j+1,k})+f(u^{\rm SW}_{j+1,k})\Big]+\\ &+\frac{a^+_{j+\frac{1}{2},k}a^-_{j+\frac{1}{2},k}}{6(a^+_{j+\frac{1}{2},k}-a^-_{j+\frac{1}{2},k})}\Big[u^{\rm NW}_{j+1,k}-u^{\rm NE}_{j,k}+4(u^{\rm W}_{j+1,k}-u^{\rm E}_{j,k})+u^{\rm SW}_{j+1,k}-u^{\rm SE}_{j,k}\Big],\end{aligned} \tag{2.14}$$

and

$$\begin{aligned}H^y_{j,k+\frac{1}{2}} &:= \frac{b^+_{j,k+\frac{1}{2}}}{6(b^+_{j,k+\frac{1}{2}}-b^-_{j,k+\frac{1}{2}})}\Big[g(u^{\rm NW}_{j,k})+4g(u^{\rm N}_{j,k})+g(u^{\rm NE}_{j,k})\Big]-\\ &-\frac{b^-_{j,k+\frac{1}{2}}}{6(b^+_{j,k+\frac{1}{2}}-b^-_{j,k+\frac{1}{2}})}\Big[g(u^{\rm SW}_{j,k+1})+4g(u^{\rm S}_{j,k+1})+g(u^{\rm SE}_{j,k+1})\Big]+\\ &+\frac{b^+_{j,k+\frac{1}{2}}b^-_{j,k+\frac{1}{2}}}{6(b^+_{j,k+\frac{1}{2}}-a^-_{j,k+\frac{1}{2}})}\Big[u^{\rm SW}_{j,k+1}-u^{\rm NW}_{j,k}+4(u^{\rm S}_{j,k+1}-u^{\rm N}_{j,k})+u^{\rm SE}_{j,k+1}-u^{\rm NE}_{j,k}\Big].\end{aligned} \tag{2.15}$$

In (2.14)–(2.15), the one-sided local speeds $a^\pm_{j+\frac{1}{2},k}, b^\pm_{j,k+\frac{1}{2}}$ are defined in (2.8), and the values of the u's are computed in (2.7) and (2.11), using the piecewise quadratic reconstruction $\{p_{j,k}\}$ at time t.

Remarks.

1. Time integration. All the aforementioned schemes, (2.4),(2.9)–(2.10); (2.4),(2.12)–(2.13) and (2.4),(2.14)–(2.15) are semi-discrete schemes. To solve the corresponding systems of time dependent ODEs, one may use any stable ODE solver. In the examples below, we use the second-order modified Euler and the third-order TVD Runge-Kutta method ([27, 26]) in connection with the second- and third-order schemes, respectively.

2. Simplicity. The Godunov-type *central* schemes enjoy the particular advantage that the computation of the midvalues in (2.7) and (2.11) is based on *component-wise* evaluation of the numerical derivatives (2.6). Consequently, no (approximate) Riemann problem solvers are required, and the intricate and time consuming part of computing the eigen-system of the problem at hand is avoided. In this sense, the simplicity offered by the above semi-discrete central schemes coupled with one's favorite ODEs solvers, leads to a class of easily implemented black-box methods for solving one- and two-dimensional systems of conservation laws and related equations governing the evolution of large gradient phenomena (see [13, 9, 14, 11, 10]).

3. Upwinding. At the same time that the schemes described above are central schemes (in the sense of realizing their solution in terms of cell averages which are integrated *across* Riemann fans), these schemes also have in common with schemes in the upwind class in the sense of following the propagation of waves emanating from the interfaces of discontinuities. Indeed, these schemes are termed as *central-upwind* schemes in [10].

   To illustrate this, one may consider the scalar linear advection equation, $u_t + au_x + bu_y = 0$ with, for example, positive constants a and b. Then the first-order version of the central-upwind scheme becomes a standard first-order upwind scheme,

$$\frac{d}{dt}u_{j,k}(t) = -a\frac{u_{j,k} - u_{j-1,k}}{\Delta x} - b\frac{u_{j,k} - u_{j,k-1}}{\Delta y}.$$

4. Multidimensional approach. The second-order scheme (2.4),(2.9)–(2.10) can also be obtained using the so-called 'dimension-by-dimension' approach, namely, by adding the corresponding one-dimensional central fluxes (similar to the derivation of multidimensional schemes in [13, 9]).

   The third-order scheme (2.4),(2.14)–(2.15), like the second-order scheme (2.4),(2.12)–(2.13), however, are *genuinely multidimensional* due to the additional cross diagonal terms, for details see [11, 10]. The performed numerical experiments indicate that the genuinely multidimensional second-order scheme (2.4),(2.12)–(2.13) is more stable and less sensitive to a choice of piecewise linear reconstruction than the 'dimension-by-dimension' scheme (2.4),(2.9)–(2.10).

5. Maximum principle. In the scalar case, both second-order schemes (2.4),(2.9)–(2.10) and (2.4),(2.12)–(2.13), coupled with the non-oscillatory minmod reconstruction (2.2)–(2.6), satisfy the maximum principle ([10, Theorem 3.1]).

3 Numerical experiments

Let us consider the two-dimensional Euler equations of gas dynamics,

$$\frac{\partial}{\partial t}\begin{bmatrix}\rho\\ \rho u\\ \rho v\\ E\end{bmatrix} + \frac{\partial}{\partial x}\begin{bmatrix}\rho u\\ \rho u^2+p\\ \rho uv\\ u(E+p)\end{bmatrix} + \frac{\partial}{\partial y}\begin{bmatrix}\rho v\\ \rho uv\\ \rho v^2+p\\ v(E+p)\end{bmatrix} = 0, \qquad p = (\gamma-1)\cdot\left[E - \frac{\rho}{2}(u^2+v^2)\right], \quad (3.1)$$

for an ideal gas, $\gamma = 1.4$. Here ρ, u, v, p and E are the density, the x- and y-velocities, the pressure and the total energy, respectively.

We solve the Riemann problem for (3.1) with initial data

$$(p,\rho,u,v)(x,y,0) = \begin{cases} (p_1,\rho_1,u_1,v_1), & \text{if } x > 0.5 \text{ and } y > 0.5, \\ (p_2,\rho_2,u_2,v_2), & \text{if } x < 0.5 \text{ and } y > 0.5, \\ (p_3,\rho_3,u_3,v_3), & \text{if } x < 0.5 \text{ and } y < 0.5, \\ (p_4,\rho_4,u_4,v_4), & \text{if } x > 0.5 \text{ and } y < 0.5. \end{cases} \tag{3.2}$$

According to [1, 16], there are 19 genuinely different admissible configurations for polytropic gas, separated by the three types of 1-D centered waves, namely, rarefaction- ($\overrightarrow{R}$), shock- ($\overrightarrow{S}$) and contact-wave ($\overrightarrow{J}$). Consult [30, 24, 25, 2]) for details.

In this Section, we compute all these solutions using the second- and third-order genuinely multidimensional central schemes, (2.4),(2.12)–(2.13) and (2.4),(2.14)–(2.15). The CFL number used is 0.475. Our numerical examples below show the density contour lines subject to 19 different initial data configurations, the same initial configurations as in [16], and we refer the reader to Schultz-Rinne et. al. [25] for a detailed discussion on the wave formation in each of these configurations.

Below, we make brief comments for each configuration, comparing our computed results with the upwind computations in [25] and [16]. Overall, our results based on central schemes reveal the same detailed information on the variety of wave formations, in a complete agreement with the upwind schemes. It is rather remarkable that this amount of details is revealed *without* any input on the 1-D elementary waves involved, beyond the maximal local speeds. The high resolution in the central and upwind approaches is comparable, with the only noticeable difference in contacts and slip lines. As expected, the resolution of the corresponding linear waves by the upwind schemes, particularly in [25], is somewhat sharper than in the central computations. The difference in resolution of these linear waves is small and in fact, in certain cases, consult Configurations 8 and 17 below, the central schemes perform better than the results reported in [16].

Configuration 1. $\begin{array}{ccc} & \overrightarrow{R_{21}} & \\ \overrightarrow{R_{32}} & & \overrightarrow{R_{41}} \\ & \overrightarrow{R_{34}} & \end{array}$: the initial data are

$$\begin{array}{llll} p_2 = 0.4 & \rho_2 = 0.5197 & p_1 = 1 & \rho_1 = 1 \\ u_2 = -0.7259 & v_2 = 0 & u_1 = 0 & v_1 = 0 \\ & & & \\ p_3 = 0.0439 & \rho_3 = 0.1072 & p_4 = 0.15 & \rho_4 = 0.2579 \\ u_3 = -0.7259 & v_3 = -1.4045 & u_4 = 0 & v_4 = -1.4045 \end{array}$$

Comments. We recover here the same 'ripples' in the middle of the left and lower rarefactions observed in [16] and in a sharpened form in [25]. The computed front propagating in between these two rarefactions is in agreement with [16], and is sharper than the one reported in [25].

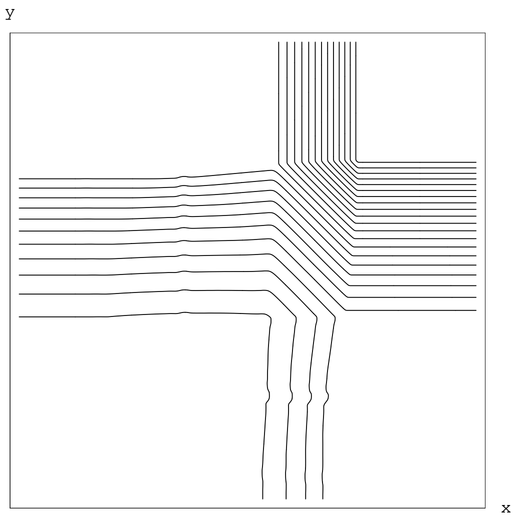

Figure 3.1a: 2-order scheme, $\theta = 2$, **T=0.2**

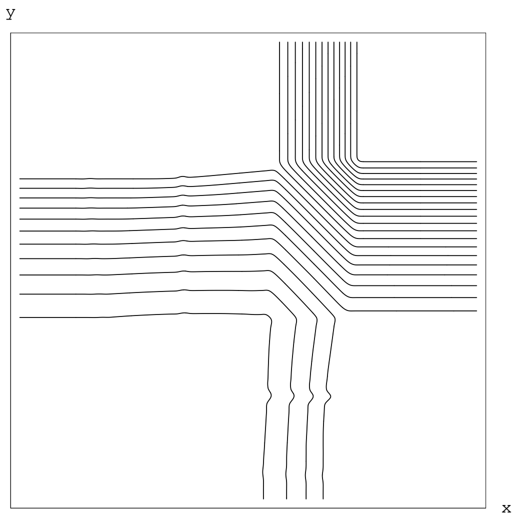

Figure 3.1b: Third-order scheme, **T=0.2**

Configuration 2. $\begin{array}{ccc} & \overrightarrow{R_{21}} & \\ \overleftarrow{R_{32}} & & \overrightarrow{R_{41}} \\ & \overleftarrow{R_{34}} & \end{array}$: the initial data are

$$\begin{array}{llll} p_2 = 0.4 & \rho_2 = 0.5197 & p_1 = 1 & \rho_1 = 1 \\ u_2 = -0.7259 & v_2 = 0 & u_1 = 0 & v_1 = 0 \\ \\ p_3 = 1 & \rho_3 = 1 & p_4 = 0.4 & \rho_4 = 0.5197 \\ u_3 = -0.7259 & v_3 = -0.7259 & u_4 = 0 & v_4 = -0.7259 \end{array}$$

Comments. The θ-limiter (2.6) proves to be over-compressive with $\theta = 2$ – the spurious oscillations can be noticed on the left, Figure 3.2a, are avoided in the third-order computation on the right. The same secondary 'ripples' are observed in all the computations

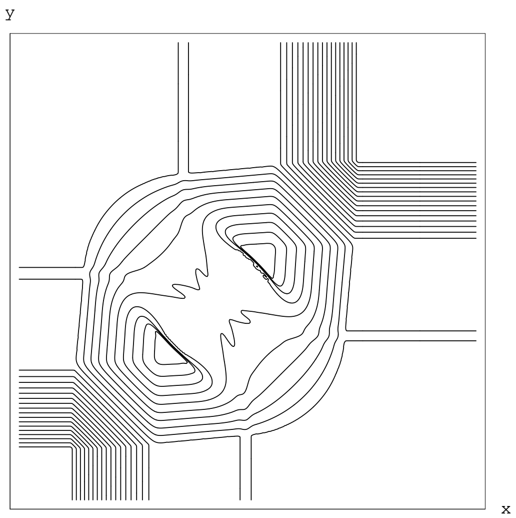

Figure 3.2a: 2-order scheme, $\theta = 2$, **T=0.2**

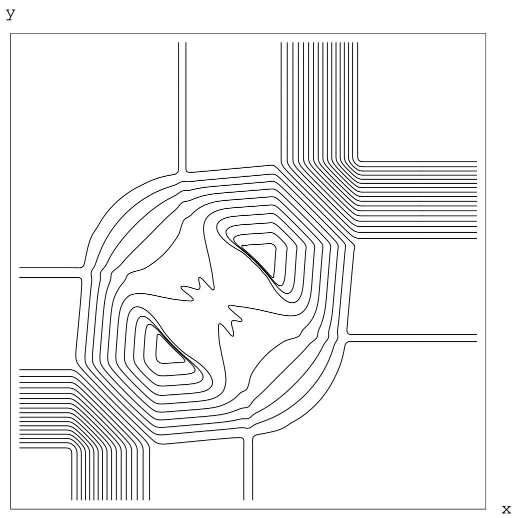

Figure 3.2b: Third-order scheme, **T=0.2**

Configuration 3. $\begin{array}{ccc} & \overleftarrow{S}_{21} & \\ \overleftarrow{S}_{32} & & \overleftarrow{S}_{41} \\ & \overleftarrow{S}_{34} & \end{array}$: the initial data are

$p_2 = 0.3$	$\rho_2 = 0.5323$	$p_1 = 1.5$	$\rho_1 = 1.5$
$u_2 = 1.206$	$v_2 = 0$	$u_1 = 0$	$v_1 = 0$
$p_3 = 0.029$	$\rho_3 = 0.138$	$p_4 = 0.3$	$\rho_4 = 0.5323$
$u_3 = 1.206$	$v_3 = 1.206$	$u_4 = 0$	$v_4 = 1.206$

Comments. As before, oscillations due to the over-compressive limiter with $\theta = 2$ in Figure 3.3a are reduced in the third-order case, and even sharper results are obtained with a more 'mild' limiter parameter, $\theta = 1$. The resolution of shocks is comparable to the upwind results.

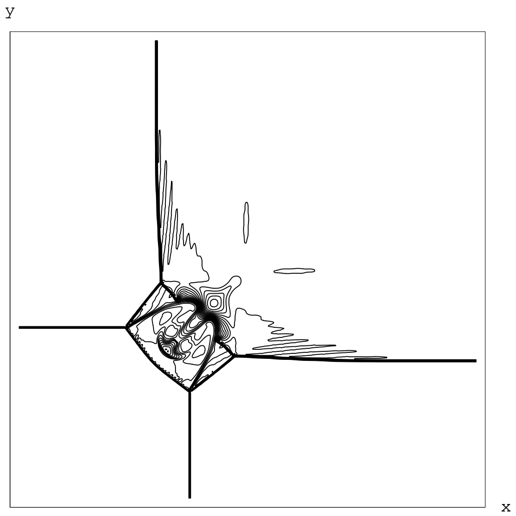

Figure 3.3a: 2-order scheme, $\theta = 2$, **T=0.3**

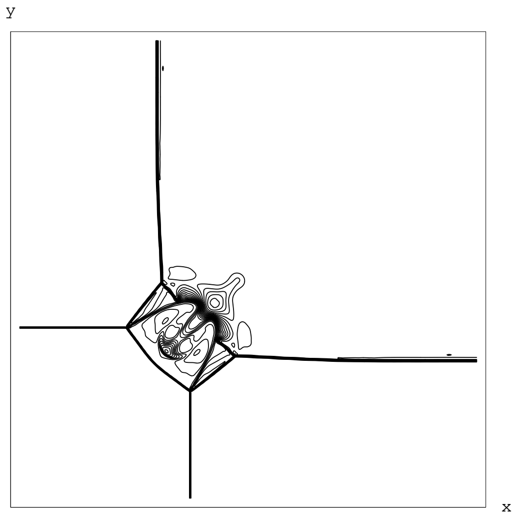

Figure 3.3b: Third-order scheme, **T=0.3**

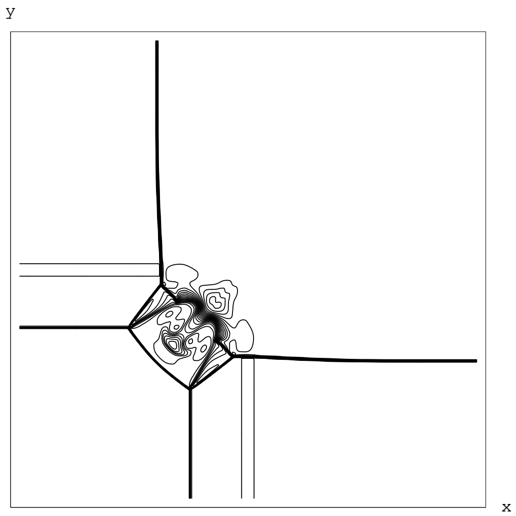

Figure 3.3c: 2-order scheme, $\theta = 1$, **T=0.3**

Configuration 4. $\begin{array}{ccc} & \overleftarrow{S_{21}} & \\ \overrightarrow{S_{32}} & & \overleftarrow{S_{41}} \\ & \overrightarrow{S_{34}} & \end{array}$: the initial data are

$p_2 = 0.35$	$\rho_2 = 0.5065$	$p_1 = 1.1$	$\rho_1 = 1.1$
$u_2 = 0.8939$	$v_2 = 0$	$u_1 = 0$	$v_1 = 0$
$p_3 = 1.1$	$\rho_3 = 1.1$	$p_4 = 0.35$	$\rho_4 = 0.5065$
$u_3 = 0.8939$	$v_3 = 0.8939$	$u_4 = 0$	$v_4 = 0.8939$

Comments. Again, $\theta = 2$ is over-compressive in Figure 3.4a, the oscillations are reduced in the third-order approximation, and sharp results, in complete agreement with those of [25, 16], are obtained with the usual minmod limiter, corresponding to $\theta = 1$.

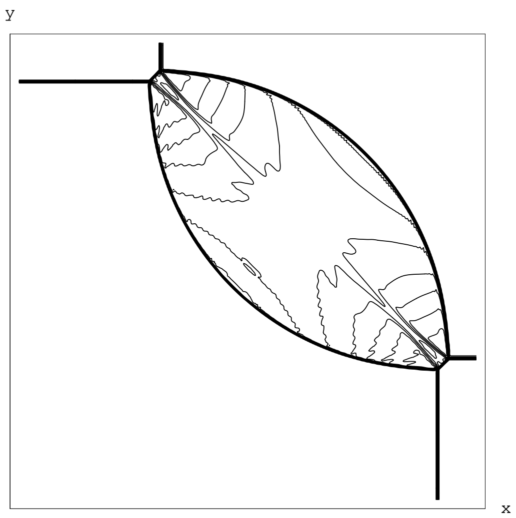

Figure 3.4a: 2-order scheme, $\theta = 2$, **T=0.25**

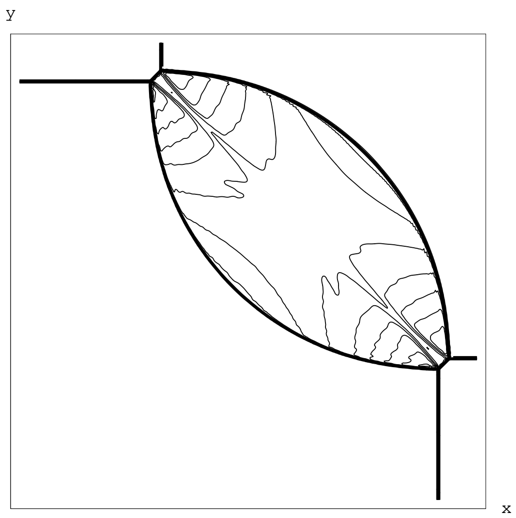

Figure 3.4b: Third-order scheme, **T=0.25**

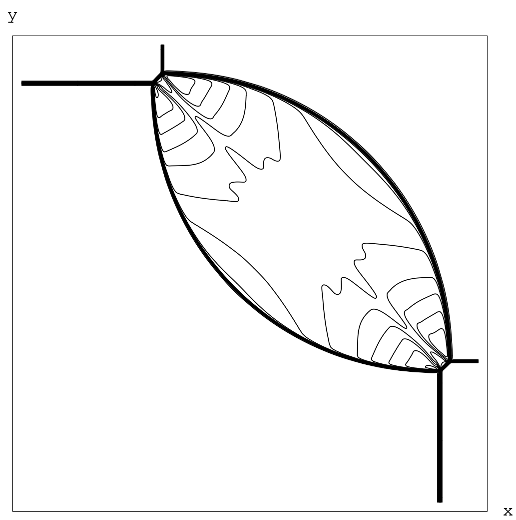

Figure 3.4c: 2-order scheme, $\theta = 1$, **T=0.25**

Configuration 5. $\begin{matrix} & J_{21}^{-} & \\ J_{32}^{-} & & J_{41}^{-} \\ & J_{34}^{-} & \end{matrix}$: the initial data are

$$\begin{array}{llll} p_2 = 1 & \rho_2 = 2 & p_1 = 1 & \rho_1 = 1 \\ u_2 = -0.75 & v_2 = 0.5 & u_1 = -0.75 & v_1 = -0.5 \\ & & & \\ p_3 = 1 & \rho_3 = 1 & p_4 = 1 & \rho_4 = 3 \\ u_3 = 0.75 & v_3 = 0.5 & u_4 = 0.75 & v_4 = -0.5 \end{array}$$

Comments. Same features are picked up by al methods, with similar resolution as in [16]. The contact obtained in [25] has a better resolution.

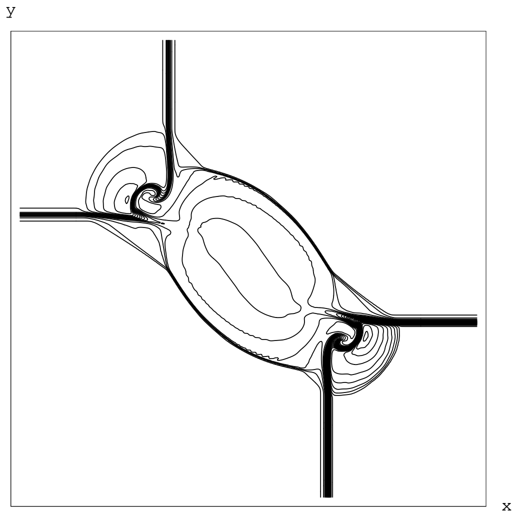

Figure 3.5a: 2-order scheme, $\theta = 1.3$, **T=0.23**

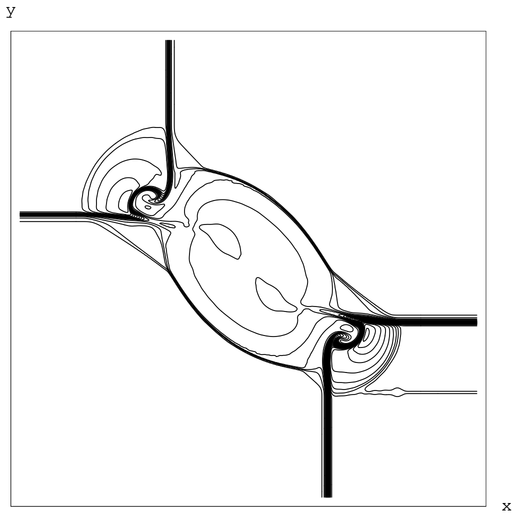

Figure 3.5b: Third-order scheme, **T=0.23**

Configuration 6. $\begin{matrix} & J_{21}^{-} & \\ J_{32}^{+} & & J_{41}^{+} \\ & J_{34}^{-} & \end{matrix}$: the initial data are

$$\begin{array}{llll} p_2 = 1 & \rho_2 = 2 & p_1 = 1 & \rho_1 = 1 \\ u_2 = 0.75 & v_2 = 0.5 & u_1 = 0.75 & v_1 = -0.5 \\ & & & \\ p_3 = 1 & \rho_3 = 1 & p_4 = 1 & \rho_4 = 3 \\ u_3 = -0.75 & v_3 = 0.5 & u_4 = -0.75 & v_4 = -0.5 \end{array}$$

Comments. The 'ripples' observed in both the NE and SW quadrants, are recovered with a comparable resolution to the one in [25, 16].

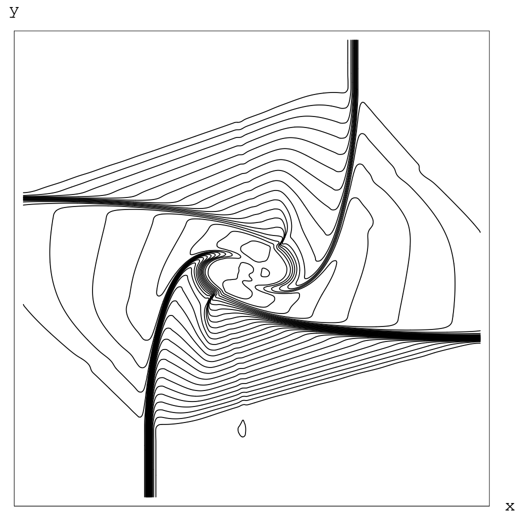

Figure 3.6a: 2-order scheme, $\theta = 1.3$, **T=0.3**

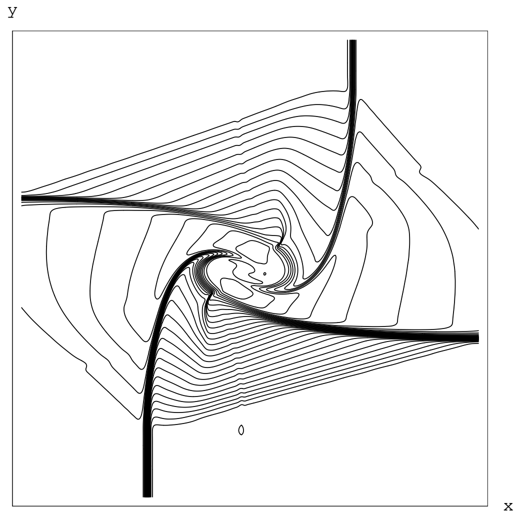

Figure 3.6b: Third-order scheme, **T=0.3**

Configuration 7. $\begin{array}{ccc} & \overrightarrow{R_{21}} & \\ J_{32}^{-} & & \overrightarrow{R_{41}} \\ & J_{34}^{-} & \end{array}$: the initial data are

$$\begin{array}{llll} p_2 = 0.4 & \rho_2 = 0.5197 & p_1 = 1 & \rho_1 = 1 \\ u_2 = -0.6259 & v_2 = 0.1 & u_1 = 0.1 & v_1 = 0.1 \\ & & & \\ p_3 = 0.4 & \rho_3 = 0.8 & p_4 = 0.4 & \rho_4 = 0.5197 \\ u_3 = 0.1 & v_3 = 0.1 & u_4 = 0.1 & v_4 = -0.6259 \end{array}$$

Comments. The high-resolution is in agreement with the corresponding upwind results in [16]. The contacts in [25] are sharper.

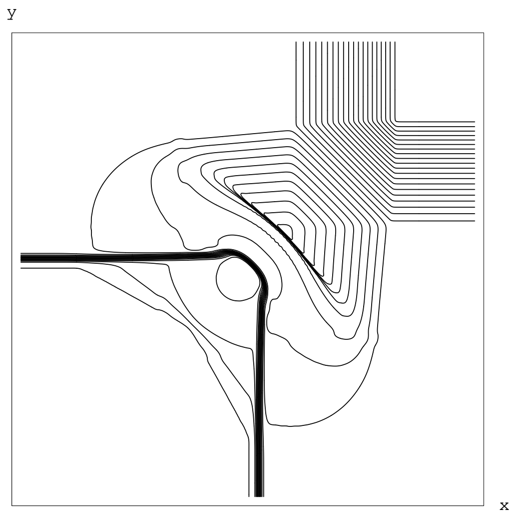

Figure 3.7a: 2-order scheme, $\theta = 1.3$, **T=0.25**

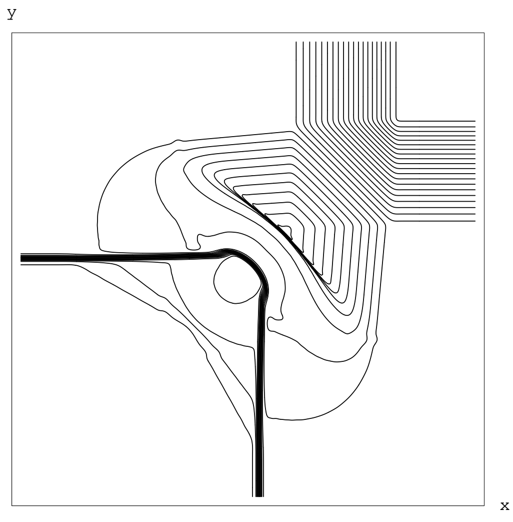

Figure 3.7b: Third-order scheme, **T=0.25**

Configuration 8. $\begin{array}{ccc} & \overleftarrow{R}_{21} & \\ J^-_{32} & & \overleftarrow{R}_{41} \\ & J^-_{34} & \end{array}$: the initial data are

$$
\begin{array}{llll}
p_2 = 1 & \rho_2 = 1 & p_1 = 0.4 & \rho_1 = 0.5197 \\
u_2 = -0.6259 & v_2 = 0.1 & u_1 = 0.1 & v_1 = 0.1 \\
 & & & \\
p_3 = 1 & \rho_3 = 0.8 & p_4 = 1 & \rho_4 = 1 \\
u_3 = 0.1 & v_3 = 0.1 & u_4 = 0.1 & v_4 = -0.6259
\end{array}
$$

Comments. The semi-circular wavefront is recovered here with sharper resolution than the one in [16], mainly due to the 'genuinely multidimensional' approach taken here, in term of the cross diagonal differences. Again, the bottom and left contacts are sharper in [25].

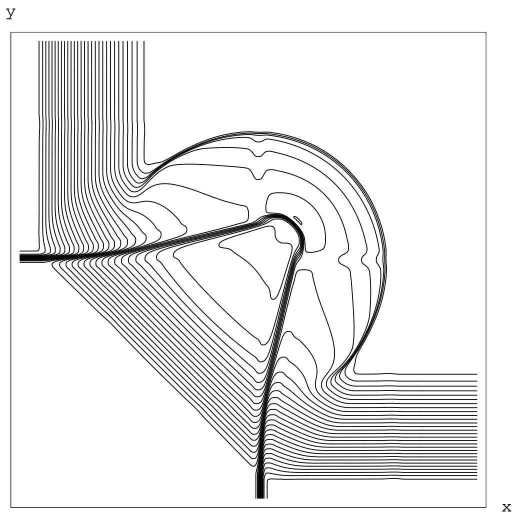

Figure 3.8a: 2-order scheme, $\theta = 1.3$, **T=0.25**

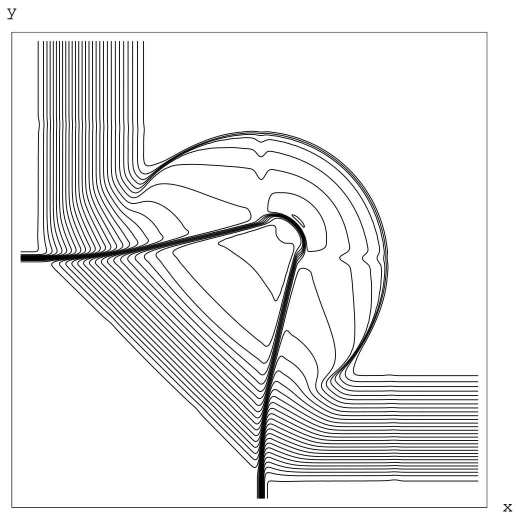

Figure 3.8b: Third-order scheme, **T=0.25**

Configuration 9. $\begin{array}{ccc} & J^+_{21} & \\ \overrightarrow{R}_{32} & & \overrightarrow{R}_{41} \\ & J^+_{34} & \end{array}$: the initial data are

$$
\begin{array}{llll}
p_2 = 1 & \rho_2 = 2 & p_1 = 1 & \rho_1 = 1 \\
u_2 = 0 & v_2 = -0.3 & u_1 = 0 & v_1 = 0.3 \\
 & & & \\
p_3 = 0.4 & \rho_3 = 1.039 & p_4 = 0.4 & \rho_4 = 0.5197 \\
u_3 = 0 & v_3 = -0.8133 & u_4 = 0 & v_4 = -0.4259
\end{array}
$$

Comments. As typical with the upwind approach, contacts are resolved better in [25, 16]. The 'bulge' on the SW corner is identical in both central and upwind computations.

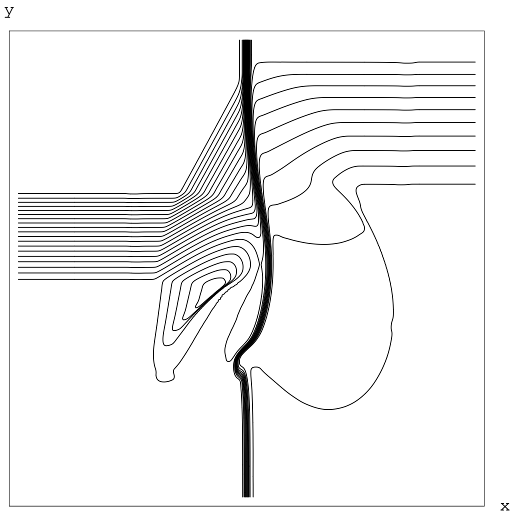

Figure 3.9a: 2-order scheme, $\theta = 1.3$, **T=0.3**

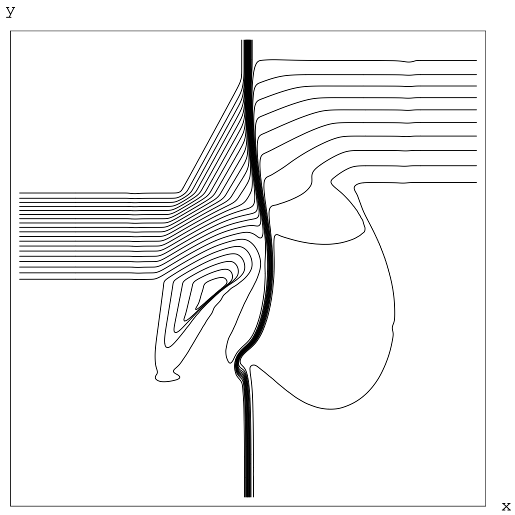

Figure 3.9b: Third-order scheme, **T=0.3**

Configuration 10. $\begin{array}{ccc} & J_{21}^- & \\ \overrightarrow{R_{32}} & & \overrightarrow{R_{41}} \\ & J_{34}^+ & \end{array}$: the initial data are

$$\begin{array}{llll} p_2 = 1 & \rho_2 = 0.5 & p_1 = 1 & \rho_1 = 1 \\ u_2 = 0 & v_2 = 0.6076 & u_1 = 0 & v_1 = 0.4297 \\ & & & \\ p_3 = 0.3333 & \rho_3 = 0.2281 & p_4 = 0.3333 & \rho_4 = 0.4562 \\ u_3 = 0 & v_3 = -0.6076 & u_4 = 0 & v_4 = -0.4297 \end{array}$$

Comments. There is a sharp resolution of the contact waves, but the resolution in [16] is somewhat better.

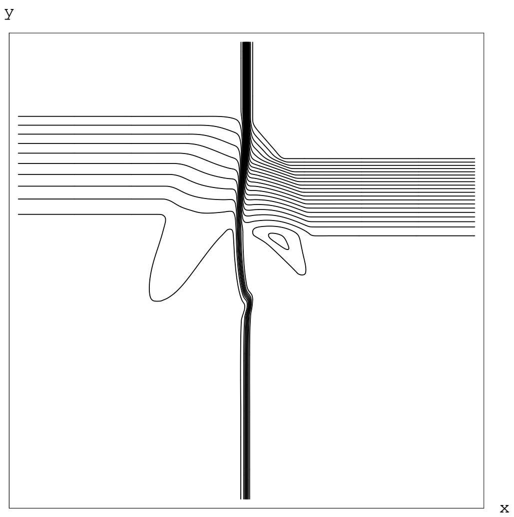

Figure 3.10a: 2-order scheme, $\theta = 1.3$, **T=0.15**

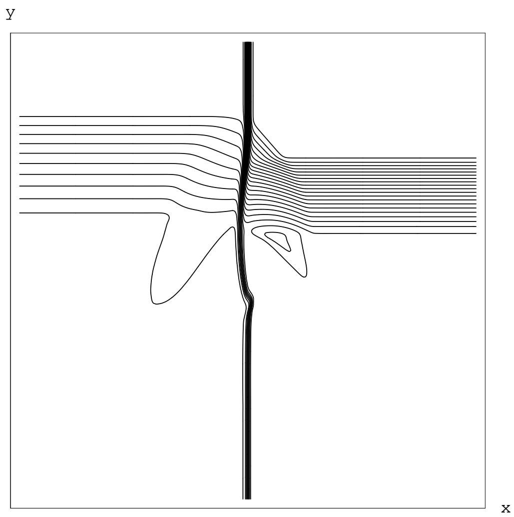

Figure 3.10b: Third-order scheme, **T=0.15**

Configuration 11. $\begin{array}{ccc} & \overleftarrow{S_{21}} & \\ J_{32}^{+} & & \overleftarrow{S_{41}} \\ & J_{34}^{+} & \end{array}$: the initial data are

$$\begin{array}{llll} p_2 = 0.4 & \rho_2 = 0.5313 & p_1 = 1 & \rho_1 = 1 \\ u_2 = 0.8276 & v_2 = 0 & u_1 = 0.1 & v_1 = 0 \\ & & & \\ p_3 = 0.4 & \rho_3 = 0.8 & p_4 = 0.4 & \rho_4 = 0.5313 \\ u_3 = 0.1 & v_3 = 0 & u_4 = 0.1 & v_4 = 0.7276 \end{array}$$

Comments. The 'ripples' in the NE quadrant are captured in full agreement with [16]. The same results are strongly peaked in [25]. The limiter parameter $\theta = 1.3$ as well as the third-order results lead to oscillations which are avoided with the standard minmod ($\theta = 1$) limiter. The contact on the left, however, is further smeared compared with [25, 16].

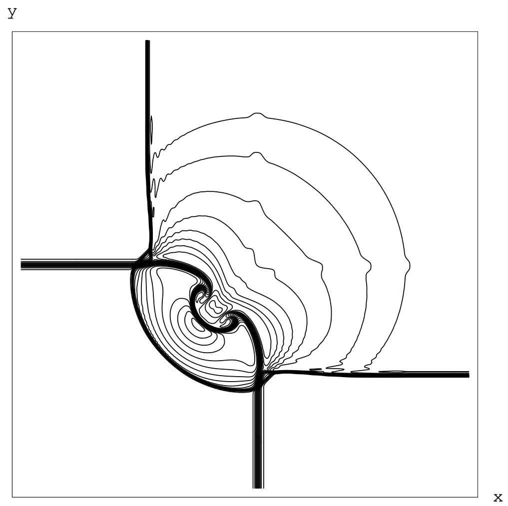

Figure 3.11a: 2-order scheme, $\theta = 1.3$, **T=0.3**

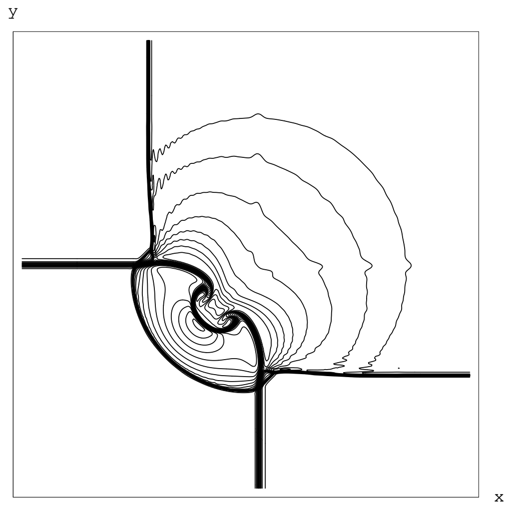

Figure 3.11b: Third-order scheme, **T=0.3**

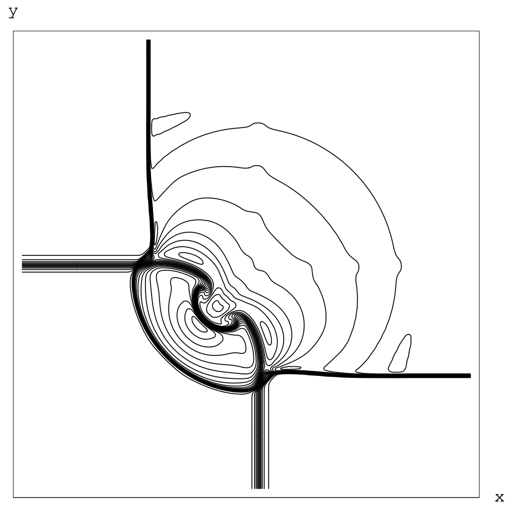

Figure 3.11c: 2-order scheme, $\theta = 1$, **T=0.3**

Configuration 12. $\begin{array}{ccc} & \overrightarrow{S_{21}} & \\ J_{32}^{+} & & \overrightarrow{S_{41}} \\ & J_{34}^{+} & \end{array}$: the initial data are

$$\begin{array}{llll} p_2 = 1 & \rho_2 = 1 & p_1 = 0.4 & \rho_1 = 0.5313 \\ u_2 = 0.7276 & v_2 = 0 & u_1 = 0 & v_1 = 0 \\ & & & \\ p_3 = 1 & \rho_3 = 0.8 & p_4 = 1 & \rho_4 = 1 \\ u_3 = 0 & v_3 = 0 & u_4 = 0 & v_4 = 0.7276 \end{array}$$

Comments. The resolution of the two contacts is improved by the third-order scheme, compared to the second-order one. The results are in agreement with upwind computations.

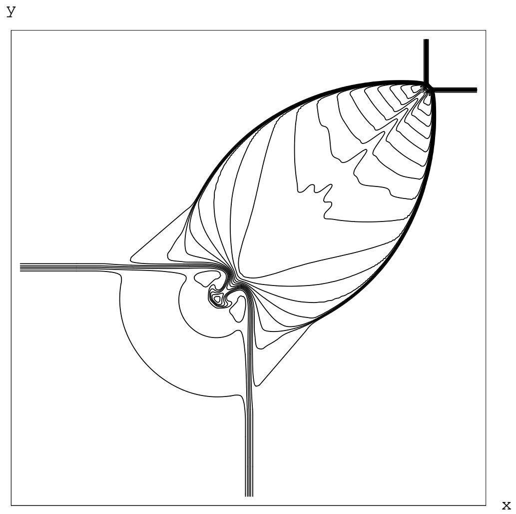

Figure 3.12a: 2-order scheme, $\theta = 1.3$, **T=0.25**

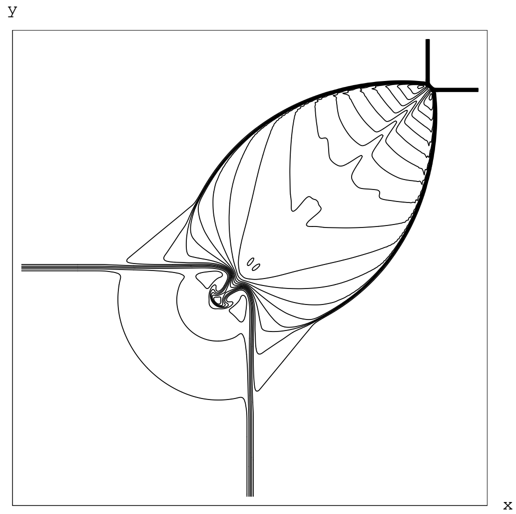

Figure 3.12b: Third-order scheme, **T=0.25**

Configuration 13. $\begin{array}{ccc} & J_{21}^{-} & \\ \overleftarrow{S_{32}} & & \overleftarrow{S_{41}} \\ & J_{34}^{-} & \end{array}$: the initial data are

$$\begin{array}{llll} p_2 = 1 & \rho_2 = 2 & p_1 = 1 & \rho_1 = 1 \\ u_2 = 0 & v_2 = 0.3 & u_1 = 0 & v_1 = -0.3 \\ & & & \\ p_3 = 0.4 & \rho_3 = 1.0625 & p_4 = 0.4 & \rho_4 = 0.5313 \\ u_3 = 0 & v_3 = 0.8145 & u_4 = 0 & v_4 = 0.4276 \end{array}$$

Comments. Does the 'blip' in the NE quadrant should be there? Indeed, this is in agreement with [25] and [16].

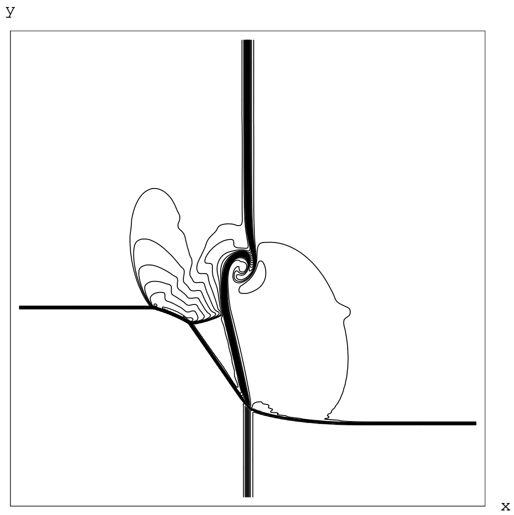

Figure 3.13a: 2-order scheme, $\theta = 1.3$, **T=0.3**

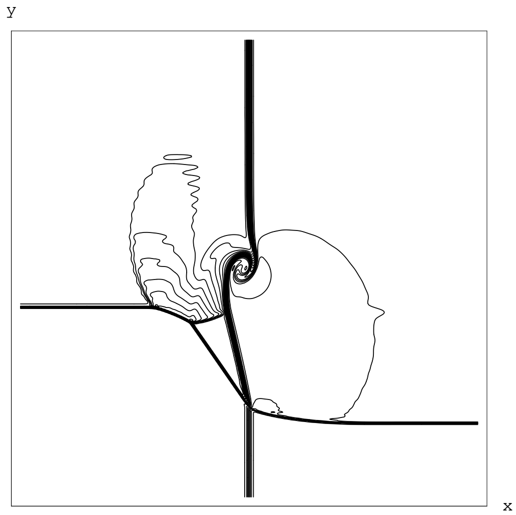

Figure 3.13b: Third-order scheme, **T=0.3**

Configuration 14. $\begin{array}{ccc} & J_{21}^{+} & \\ \overleftarrow{S}_{32} & & \overleftarrow{S}_{41} \\ & J_{34}^{-} & \end{array}$: the initial data are

$$\begin{array}{llll} p_2 = 8 & \rho_2 = 1 & p_1 = 8 & \rho_1 = 2 \\ u_2 = 0 & v_2 = -1.2172 & u_1 = 0 & v_1 = -0.5606 \\ & & & \\ p_3 = 2.6667 & \rho_3 = 0.4736 & p_4 = 2.6667 & \rho_4 = 0.9474 \\ u_3 = 0 & v_3 = 1.2172 & u_4 = 0 & v_4 = 1.1606 \end{array}$$

Comments. The resolution of the contact in [16] is slightly sharper than the one achieved by the central scheme.

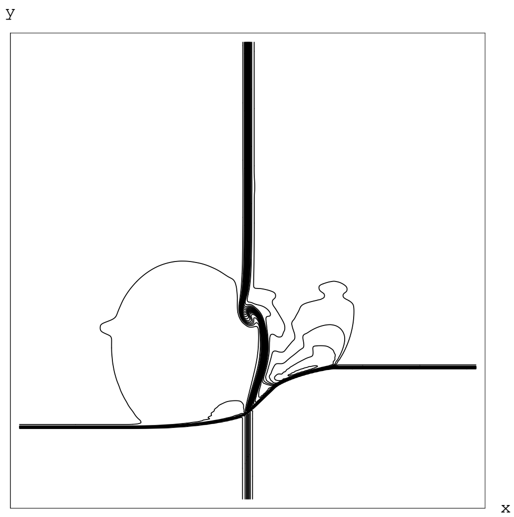

Figure 3.14a: 2-order scheme, $\theta = 1.3$, **T=0.1**

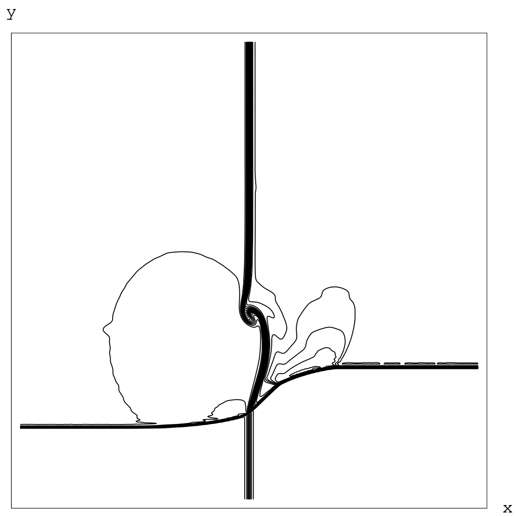

Figure 3.14b: Third-order scheme, **T=0.1**

Configuration 15. $\begin{array}{ccc} & \overrightarrow{R}_{21} & \\ J_{32}^{-} & & \overleftarrow{S}_{41} \\ & J_{34}^{+} & \end{array}$: the initial data are

$$\begin{array}{llll} p_2 = 0.4 & \rho_2 = 0.5197 & p_1 = 1 & \rho_1 = 1 \\ u_2 = -0.6259 & v_2 = -0.3 & u_1 = 0.1 & v_1 = -0.3 \\ & & & \\ p_3 = 0.4 & \rho_3 = 0.8 & p_4 = 0.4 & \rho_4 = 0.5313 \\ u_3 = 0.1 & v_3 = -0.3 & u_4 = 0.1 & v_4 = 0.4276 \end{array}$$

Comments. Again, the sharp resolution of the contacts is only slightly less than those in [16]. The lower contact in [25] is sharper, but our results is free of the weak oscillations observed in [25] at the tip of the shock.

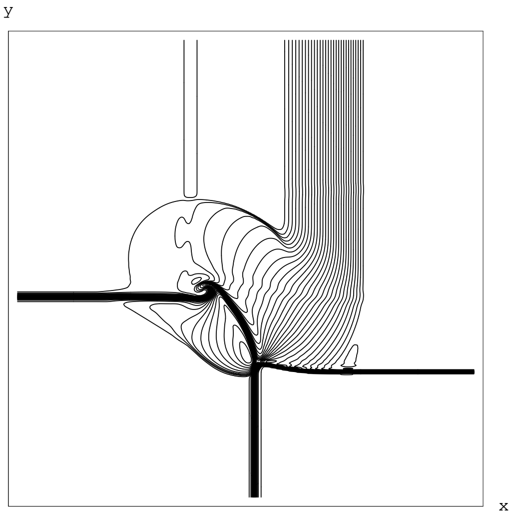

Figure 3.15a: 2-order scheme, $\theta = 1.3$, **T=0.2**

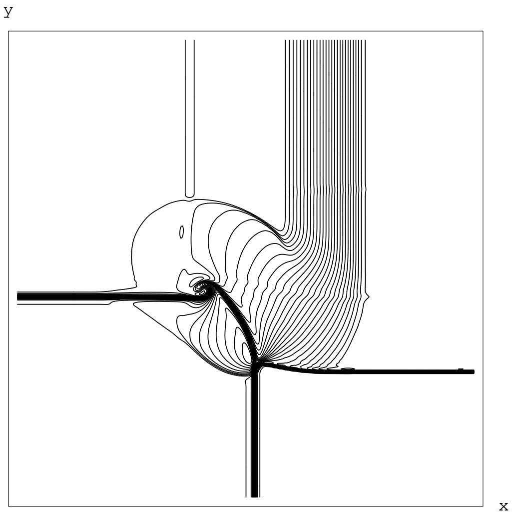

Figure 3.15b: Third-order scheme, **T=0.2**

Configuration 16. $\begin{array}{ccc} & \overleftarrow{R}_{21} & \\ J_{32}^{-} & & \overrightarrow{S}_{41} \\ & J_{34}^{+} & \end{array}$: the initial data are

$$\begin{array}{llll} p_2 = 1 & \rho_2 = 1.0222 & p_1 = 0.4 & \rho_1 = 0.5313 \\ u_2 = -0.6179 & v_2 = 0.1 & u_1 = 0.1 & v_1 = 0.1 \\ & & & \\ p_3 = 1 & \rho_3 = 0.8 & p_4 = 1 & \rho_4 = 1 \\ u_3 = 0.1 & v_3 = 0.1 & u_4 = 0.1 & v_4 = 0.8276 \end{array}$$

Comments. The 'ripples', observed between the shock and contact waves, reproduce the same waveform as in [25, 16]. Here, the shock resolution in [25] is sharper than [16] and the result in Figure 3.16b.

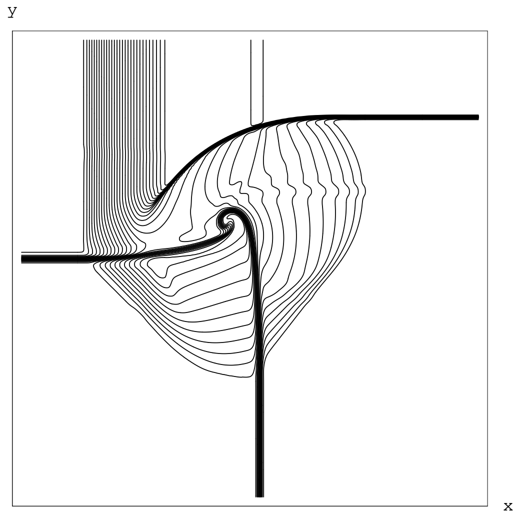

Figure 3.16a: 2-order scheme, $\theta = 1.3$, **T=0.2**

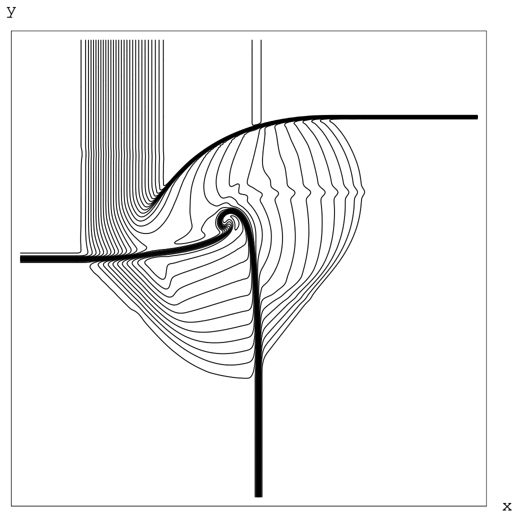

Figure 3.16b: Third-order scheme, **T=0.2**

Configuration 17. $\begin{array}{ccc} & J_{21}^{-} & \\ \overleftarrow{S_{32}} & & \overrightarrow{R_{41}} \\ & J_{34}^{-} & \end{array}$: the initial data are

$$\begin{array}{llll} p_2 = 1 & \rho_2 = 2 & p_1 = 1 & \rho_1 = 1 \\ u_2 = 0 & v_2 = -0.3 & u_1 = 0 & v_1 = -0.4 \\ & & & \\ p_3 = 0.4 & \rho_3 = 1.0625 & p_4 = 0.4 & \rho_4 = 0.5197 \\ u_3 = 0 & v_3 = 0.2145 & u_4 = 0 & v_4 = -1.1259 \end{array}$$

Comments. Here, we obtain sharp resolution of the contact without the spurious vorticities appearing in [16]. In both cases, one observes the 'ripple' formed in the NW quadrant.

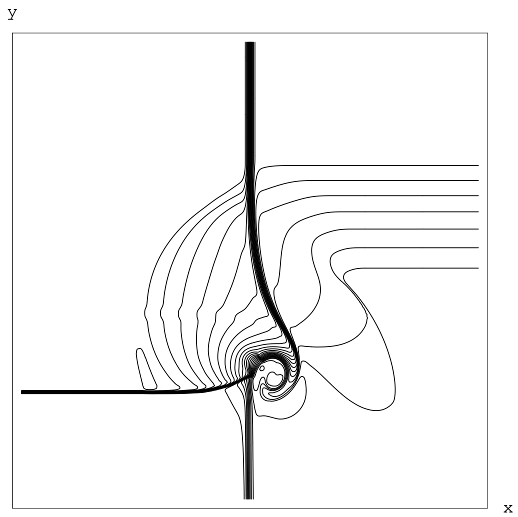

Figure 3.17a: 2-order scheme, $\theta = 1.3$, **T=0.3**

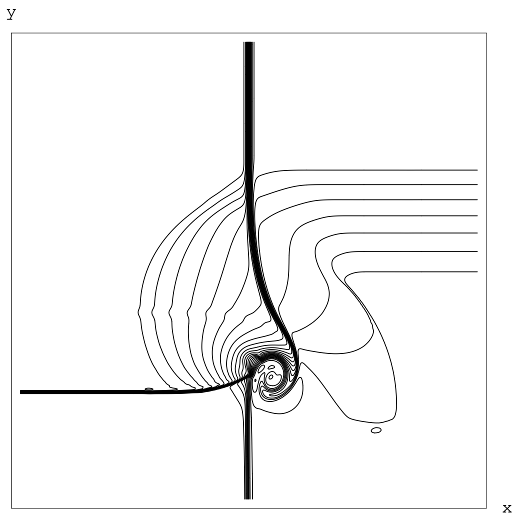

Figure 3.17b: Third-order scheme, **T=0.3**

Configuration 18. $\begin{array}{ccc} & J_{21}^{+} & \\ \overleftarrow{S_{32}} & & \overrightarrow{R_{41}} \\ & J_{34}^{+} & \end{array}$: the initial data are

$$\begin{array}{llll} p_2 = 1 & \rho_2 = 2 & p_1 = 1 & \rho_1 = 1 \\ u_2 = 0 & v_2 = -0.3 & u_1 = 0 & v_1 = 1 \\ & & & \\ p_3 = 0.4 & \rho_3 = 1.0625 & p_4 = 0.4 & \rho_4 = 0.5197 \\ u_3 = 0 & v_3 = 0.2145 & u_4 = 0 & v_4 = 0.2741 \end{array}$$

Comments. The resolution of the contacts is almost as sharp as in [16]. The 'ripples' in the NW quadrant are observed in all computations.

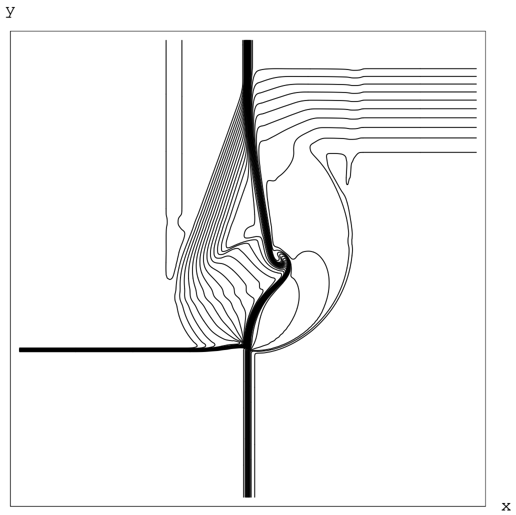

Figure 3.18a: 2-order scheme, $\theta = 1.3$, **T=0.2**

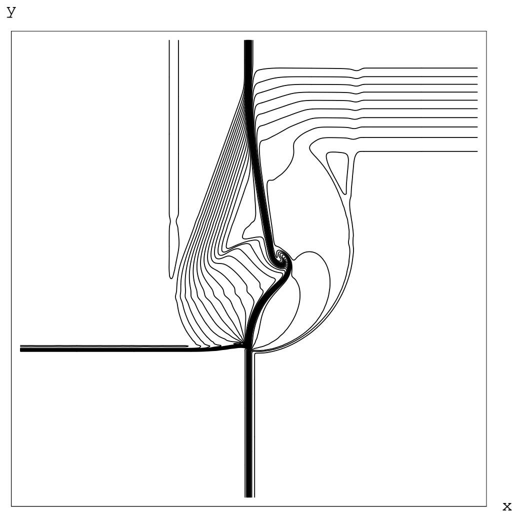

Figure 3.18b: Third-order scheme, **T=0.2**

Configuration 19. $\begin{array}{ccc} & J_{21}^{+} & \\ \overleftarrow{S_{32}} & & \overrightarrow{R_{41}} \\ & J_{34}^{-} & \end{array}$: the initial data are

$$\begin{array}{llll} p_2 = 1 & \rho_2 = 2 & p_1 = 1 & \rho_1 = 1 \\ u_2 = 0 & v_2 = -0.3 & u_1 = 0 & v_1 = 0.3 \\ & & & \\ p_3 = 0.4 & \rho_3 = 1.0625 & p_4 = 0.4 & \rho_4 = 0.5197 \\ u_3 = 0 & v_3 = 0.2145 & u_4 = 0 & v_4 = -0.4259 \end{array}$$

Comments. As before – ripples are observed in NW quadrant, and only the resolution of contacts is slightly sharper in [16].

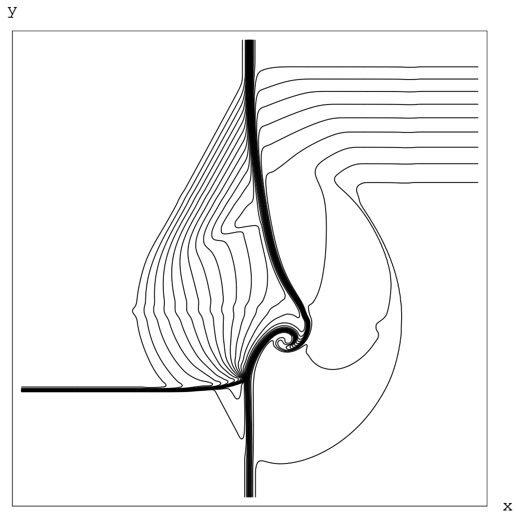

Figure 3.19a: 2-order scheme, $\theta = 1.3$, **T=0.3**

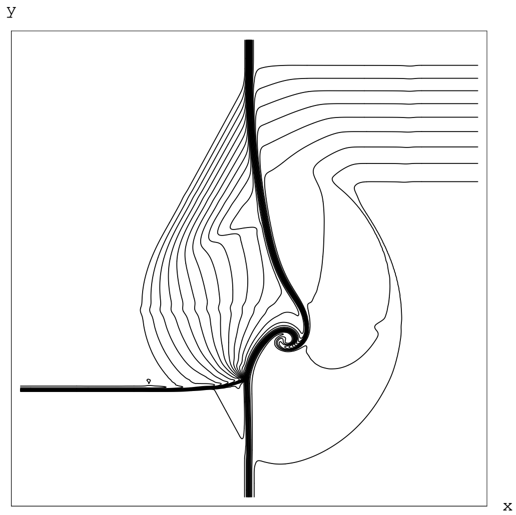

Figure 3.19b: Third-order scheme, **T=0.3**

Acknowledgment: The work of A. Kurganov was supported in part by the NSF Group Infrastructure Grant. E. tadmor was supported by ONR grant N00014-91-J-1076 and NSF grant #DMS97-06827

References

[1] T. Chang, G.-Q. Chen and S. Yang, *On the 2-D Riemann problem for the compressible Euler equations. I. Interaction of shocks and rarefaction waves*, Discrete Contin. Dynam. Systems, 1 (1995), pp. 555–584.

[2] T. Chang, G.-Q. Chen and S. Yang, *On the 2-D Riemann problem for the compressible Euler equations. I. Interaction of contact discontinuities*, Discrete Contin. Dynam. Systems, 6 (2000), pp. 419–430.

[3] S.K. Godunov, *A finite difference method for the numerical computation of discontinuous solutions of the equations of fluid dynamics*, Mat. Sb., 47 (1959), pp. 271–290.

[4] A. Harten, *High resolution schemes for hyperbolic conservation laws*, J. of Comp. Phys., 49 (1983), pp. 357–393.

[5] A. Harten, B. Engquist, S. Osher and S.R. Chakravarthy, *Uniformly high order accurate essentially non-oscillatory schemes III*, J. of Comp. Phys., 71 (1987), pp. 231–303.

[6] G.-S. Jiang and E. Tadmor, *Non-oscillatory central schemes for multidimensional hyperbolic conservation laws*, SIAM J. Sci. Comp., 19 (1998), pp. 1892–1917.

[7] S. Jin and Z. Xin, *The relaxation schemes for systems of conservation laws in arbitrary space dimensions*, CPAM **48**, 1995, pp. 235-276.

[8] A. Kurganov, *Conservation laws: stability of numerical approximations and nonlinear regularization*, Ph.D. Thesis, Tel-Aviv University, Israel (1997).

[9] A. Kurganov and D. Levy, *A third-order semi-discrete central scheme for conservation laws and convection-diffusion equations*, SIAM J. Sci. Comp., to appear.

[10] A. Kurganov, S. Noelle and G. Petrova, *Semi-discrete central-upwind scheme for hyperbolic conservation laws and Hamilton-Jacobi equations*, submitted to SISC.

[11] A. Kurganov and G. Petrova, *A third-order semi-discrete genuinely multidimensional central scheme for hyperbolic conservation laws and related problems*, Numerische Mathematik, to appear.

[12] A. Kurganov and G. Petrova, *Central Schemes and Contact Discontinuities*, Math. Model. and Numer. Anal., to appear.

[13] A. Kurganov and E. Tadmor, *New high-resolution central schemes for nonlinear conservation laws and convection-diffusion equations*, J. of Comp. Phys., 160 (2000), pp. 214–282.

[14] A. Kurganov and E. Tadmor, *New high-resolution semi-discrete central schemes for Hamilton-Jacobi equations*, J. of Comp. Phys., 160 (2000), pp. 720–742.

[15] P.D. Lax. *Weak solutions of non-nonlinear hyperbolic equations and their numerical computations*, CPAM **7**, 1954, pp. 159-193.

[16] P. Lax and X.-D. Liu, *Solution of two-dimensional Riemann problems of gas dynamics by positive schemes*, SIAM J. Sci. Comp., 19 (1998), pp. 319–340.

[17] B. van Leer, *Towards the ultimate conservative difference scheme, V. A second order sequel to Godunov's method*, J. of Comp. Phys., 32 (1979), pp. 101–136.

[18] D. Levy, G. Puppo and G. Russo, *A third order central WENO scheme for 2D conservation laws*, Appl. Numer. Math., 33 (2000), pp. 407–414.

[19] D. Levy, G. Puppo and G. Russo, *Compact central WENO schemes for multidimensional conservation laws*, SIAM J. Sci. Comp., 22 (2000) 656–672.

[20] X.-D. Liu and S. Osher, *Nonoscillatory high order accurate self similar maximum principle satisfying shock capturing schemes. I*, SIAM J. Numer. Anal., 33 (1996), pp. 760–779.

[21] X.-D. Liu and E. Tadmor, *Third order nonoscillatory central scheme for hyperbolic conservation laws*, Numerische Mathematik, 79 (1998), pp. 397–425.

[22] X.-D. Liu and S. Osher, *Convex ENO high order multi-dimensional schemes without field by field decompositions or staggered grids*, J. Comput. Phys. 142 (1998), 304–330.

[23] H. Nessyahu and E. Tadmor, *Non-oscillatory central differencing for hyperbolic conservation laws*, J. Comp. Phys., 87 (1990), pp. 408–463.

[24] C. W. Schulz-Rinne, *Classification of the Riemann problem for two-dimensional gas dynamics*, SIAM J. Math. Anal., 24 (1993), pp. 76–88.

[25] C. W. Schulz-Rinne, J. P. Collins and H. M. Glaz, *Numerical solution of the Riemann problem for two-dimensional gas dynamics*, SIAM J. Sci. Comp., 14 (1993), pp. 1394–1414.

[26] C.-W. Shu, *Total-variation-diminishing time discretizations*, SIAM J. Sci. Comp., 6 (1988), pp. 1073–1084.

[27] C.-W. SHU AND S. OSHER, *Efficient implementation of essentially non-oscillatory shock-capturing schemes*, J. Comp. Phys., 77 (1988), pp. 439–471.

[28] J. SMOLLER, *Shock waves and reaction diffusion-equations* (second edition), Grundleheren Series 258, Springer-Verlag, 1994.

[29] S. OSHER AND E. TADMOR, *On the convergence of difference approximations to scalar conservation laws*, Math. Comp., 50 (1988), pp. 19–51.

[30] T. ZHANG AND Y. ZHENG, *Conjecture on the structure of solutions of the Riemann problem for two-dimensional gas dynamics systems*, SIAM J. Math. Anal., 21 (1990), pp. 593–630.